Journal of Power Sources 238 (2013) 165–172

Contents lists available at SciVerse ScienceDirect

Journal of Power Sources

journal homepage: www.elsevier.com/locate/jpowsour

Fabrication and electrochemical properties of Si/TiO_2 nanowire array composites as lithium ion battery anodes

Zhen Wei, Ruoshi Li, Tao Huang*, Aishui Yu*

Department of Chemistry, Shanghai Key Laboratory of Molecular Catalysis and Innovative Materials, Institute of New Energy, Fudan University, Shanghai 200438, China

HIGHLIGHTS

- A novel material of TiO_2 nanowire array/Si composite has been fabricated.
- TiO_2 nanowire framework separates Si bulk apart and accommodates Si volume expansion.
- Mass ratio of Si to TiO_2 is tuned to achieve the best electrochemical performance.
- Composite with 75% Si owns the highest capacity of 802.3 mA h g^{-1} after 200 cycles.

ARTICLE INFO

Article history:
Received 7 December 2012
Received in revised form
8 March 2013
Accepted 11 March 2013
Available online 26 March 2013

Keywords:
Titania nanowire array
Solvothermal crystal growth
Silicon
Lithium ion battery anode

ABSTRACT

A novel material of Si/TiO_2 nanowire array (TNA) composite has been designed and fabricated, to be used as anode material for lithium ion batteries. Firstly, Self-assembled and well-aligned rutile TiO_2 nanowire arrays are synthesized on pretreated titanium substrate by solvothermal route. Subsequently, Si film is introduced into the interspace of the nanowires, forming a Si/TNA composite. The field-emission scanning electron microscopy (FE-SEM) and transmission electron microscope (TEM) images indicate that the dimension of TiO_2 nanowires is 10 ± 2 nm wide. The TEM and Raman results reveal that Si contains amorphous and nanocrystalline phases. The composite with 75% Si content owns the best electrochemical performance, the first charge capacity reaches as high as 1480 mA h g^{-1}, and remains at 802.3 mA h g^{-1} after 200 cycles.

1. Introduction

The performance advantages of lithium ion batteries (LIBs) are much better than those of other choices in the secondary battery market [1–4]. So LIBs have been considered the most promising energy storage technologies for mobile electronics, electric vehicles and renewable energy systems [5,6]. Among various anode materials, Si has emerged as potential anode materials for LIBs due to its high theoretical specific capacity, abundant amount on earth and low cost [7,8]. Its theoretical specific capacity (4200 mA h g^{-1}) is much larger than that of the already-commercialized graphite (372 mA h g^{-1}), However, substantial volume changes are associated with the Li alloying and de-alloying process, which causes fast crack and pulverization of Si electrode and results in rapid capacity fade. Many attempts have been made to improve the cycling ability of Si anode such as investigating nanostructured Si [9,10], doping [11,12], coating [13,14] and adding other elements (including ZrO_2, TiN, mesoporous TiO_2, Ni) to alleviate the volume change [15–22].

On the other hand, nanostructured TiO_2 has been widely investigated in the field of electrochemical energy storage [21]. It owns a very small volume expansion ratio (3%) [22] upon Li ion intercalation/extraction, and exhibits good cyclic stability [23]. Well-ordered TiO_2 nanowire arrays offer a large internal surface area and excellent pathways for Li-ion to transfer between interfaces. So it is an excellent material employed as a stable anode for lithium ion batteries. However, the theoretical specific capacity of TiO_2 is very low (168 mA h g^{-1} for $Li_{0.5}TiO_2$), restricting its use in Li ion batteries.

Herein, we design and fabricate a novel material of Si/TiO_2 nanowire array (TNA) composite, which combines the advantages of high specific capacity of Si with the structural stability of TNA. The specific capacity of TNA is greatly improved by introducing Si component. We researched on different mass percentage of Si in the Si/TNA composite, to find a best ratio of Si to TiO_2. The as-prepared Si/TNA composite is already connected to titanium

* Corresponding authors.
E-mail address: asyu@fudan.edu.cn (A. Yu).

0378-7753/$ – see front matter © 2013 Elsevier B.V. All rights reserved.
http://dx.doi.org/10.1016/j.jpowsour.2013.03.080

current collector, no need of binder and conductive agent for Li ion battery application.

2. Experimental procedure

2.1. Materials preparation

Pure titanium sheets of 14 mm in diameter and 0.3 mm in thickness were initially cleaned by ultrasonication in acetone, ethanol and deionized water for 30 min, respectively.

Before the solvothermal experiment, a compact TiO_2 nanoparticle layer was deposited onto the well cleaned titanium substrate by being immersed in a 0.05 M $TiCl_4$ aqueous solution at 70 °C for 30 min, then heated in air at 500 °C for 30 min [24]. The TNA films without a compact layer tend to peel off from the substrate due to poor adhesion.

The titanium sheet was placed into a sealed Teflon autoclave (50 mL) with the surface treated by TiO_2 compact layer facing downward. 10 mL of toluene, 1 mL of tetrabutyl titanate and 1 mL of hydrochloric acid (37 wt %) were added into the autoclave as the solvothermal solution. The solvothermal process was conducted at 180 °C for 1 h in a furnace. After the solvothermal experiment, the resulting samples were rinsed with ethanol, and then dried in air.

Introducing silicon component into the TNAs was achieved by magnetron sputtering system (Chengdu Nanguang Machine Co., Ltd.) with TNA as the substrate and Si (99.99%) as the target. The target–substrate distance of the sputtering system was 5 cm. After attaining a base pressure of 3.0×10^{-3} Pa, high-purity argon (99.999%) was introduced into the stainless-steel chamber. The working pressure was kept at 0.30 Pa. Si thin films were deposited using a constant rf power supply of 240 W. The substrate temperatures were selected as room temperature. The average loading rate is determined to be 0.5 mg Si per 1 h. We prepared 5 samples with different Si percentage in the composite, 0%, 25%, 50%, 75% and 100%.

2.2. Characterization and electrochemical measurement

The crystal structures of the samples were characterized by X-ray diffraction (XRD, Bruker D8 Advance) with Cu Ka radiation. The morphology was characterized using field emission scanning electron microscopy (FE-SEM, Hitachi S-4800) and transmission electron microscope (TEM, JEM -2100F). Raman spectra were recorded on a Raman spectrometer (Renishaw inVia Reflex) coupled with microscope in a reflectance mode with a 514.5 nm excitation laser source. The amount of the deposited Si was measured by analytical balance (Ohaus Discovery DV215CD, resolution of 0.01 mg). The mass percentage of Si in the composite was determined by analytical balance in combination with Energy-dispersive X-ray spectroscopy (EDX, Hitachi S-4800). The distribution of Si is measured by element analysis mapping (JEM-2100F).

Electrochemical tests were performed using a CR2016-type coin cell. The Si/TNAs composites on Ti substrates were used directly as the working electrode. Cell assembly was performed in a glove box (Superstar 1220/750, Mikrouna) filled with pure argon. Lithium metal was used as counter electrode and the electrolyte was 1 M $LiPF_6$ dissolved in a mixed solvent of ethylene carbonate (EC)/diethyl carbonate (DEC) (1:1 by volume). A celgard 2300 membrane was used as the cell separator. Cyclic voltammetry measurements were carried out using an electrochemical workstation (CHI 660A, Chenhua Instrument Company) between 0 and 2.7 V versus Li/Li^+ at a scan rate of 0.10 mV s^{-1}. Galvanostatic Charge/discharge experiments were performed on a battery test system (LAND CT2001A, Wuhan Jinnuo Electronic Co. Ltd, China) between 0 V and 2.7 V at 100 mA g^{-1}. In this paper, active material mass was measured by subtracting titanium mass from the total mass.

3. Results and discussion

Fig. 1 reveals the FE-SEM images of the composites with different Si percentages. After solvothermal reaction, as shown in Fig. 1(a), highly ordered, well-oriented TiO_2 nanowires are successfully fabricated, growing perpendicular to the substrate. The essential structure of these samples is a single nanowire, and several nanowires bunch together to form a secondary structure, that's a bunch of nanowires. A single nanowire is 10 ± 2 nm wide, and the nanowire bunch is 60 ± 10 nm wide. In Fig. 1(b), silicon have been sputtered into the interspace between TiO_2 nanowires, and covers the TiO_2 surface uniformly. The diameter of silicon nanoparticles is 90 ± 10 nm. As for the samples with silicon percentage above 50%, i.e. longer sputtering time, the sputtered silicon forms a glabrous film, and no particles can be identified. To verify the penetration of silicon into TiO_2 network, cross-section micrographs of the TNA and the Si(75%)/TNA composite are given in Fig. 1(f and g). For pure TiO_2, nanowires are clearly separated and run through the whole film. After adding Si component, a Si film forms on the TiO_2 surface and the nanowires become blurry. On the whole the entire TiO_2 film is covered by Si component.

Considering both aspects of high capacity and cycling stability, the composite with 75% Si owns appropriate mass ratio of Si to TiO_2, and is promising to exhibit good performance. Thus subsequent characterization is performed on this sample.

XRD patterns for TNA and Si(75%)/TNA composites are measured to characterize the crystal structure, as shown in Fig. 2(i). In the curve for TNA, diffraction peaks marked as "▲" are ascribed from tetragonal rutile TiO_2 (JCPDS No. 21-1276). Diffraction peaks at $2\theta = 36.1°$, 62.7° can be indexed to crystal planes (101), (002). All the other peaks without marks are from titanium substrate (JCPDS No. 44-1294). In the curve for Si(75%)/TNA composites, apart from the peaks of rutile TiO_2, new diffraction peak (marked as "★") emerges at $2\theta = 28.4°$, which ascribes to crystal plane (111) of Si (JCPDS No. 27-1402).

The diffraction peak is wide and the intensity is not strong, indicating that Si is composed of nanocrystalline in small size, the average dimension of crystallites d was estimated from the linewidths of selected XRD reflections by the Scherrer formula:

$$D = K\lambda/\beta\cos\theta$$

where − shape factor ($K = 0.89$), λ − incident X-ray wavelength ($\lambda_{CuK\alpha} = 1.541$ Å here), β − full width at half-maximum (FWHM) of a given line and θ − position of that line in the pattern. The average crystallite size is calculated as 1.4 nm. While Si particles observed in Fig. 1(b) is in the range of 90 ± 10 nm, and this is the secondary structure dimension.

To further verify the crystalline phase of Si, additional Raman spectroscopy is performed and shown in Fig. 2(ii). All the Raman peaks and bands of TiO_2 at 143 cm^{-1} (B_{1g}), 447 cm^{-1} (E_g), 612 cm^{-1} (A_{1g}) are consistent with its rutile phase [25]. As to Si, crystalline Si can be easily distinguished from amorphous Si as they give rise to different Raman spectra. Raman peak of Si(75%)/TNA composites appears at around 500 cm^{-1}, and it is overlapped by two peaks: 480 cm^{-1} for amorphous Si and 520 cm^{-1} for crystalline Si [26,27]. The Raman data reveals that the as-prepared composite contains two kinds of Si phase.

The Si/TiO_2 nanowire array composite structure is confirmed by TEM images as shown in Fig. 3. It is clearly seen that Si distribute uniformly at the lateral surface of nanowires, proving that Si have been successfully deposited into the interspace between the TiO_2 nanowires. In Fig. 3(a), the uncrystallized film wrapping TiO_2 is identified as amorphous Si. In Fig. 3(b), crystallized Si is verified between the TiO_2 nanowires. The distance between the adjacent

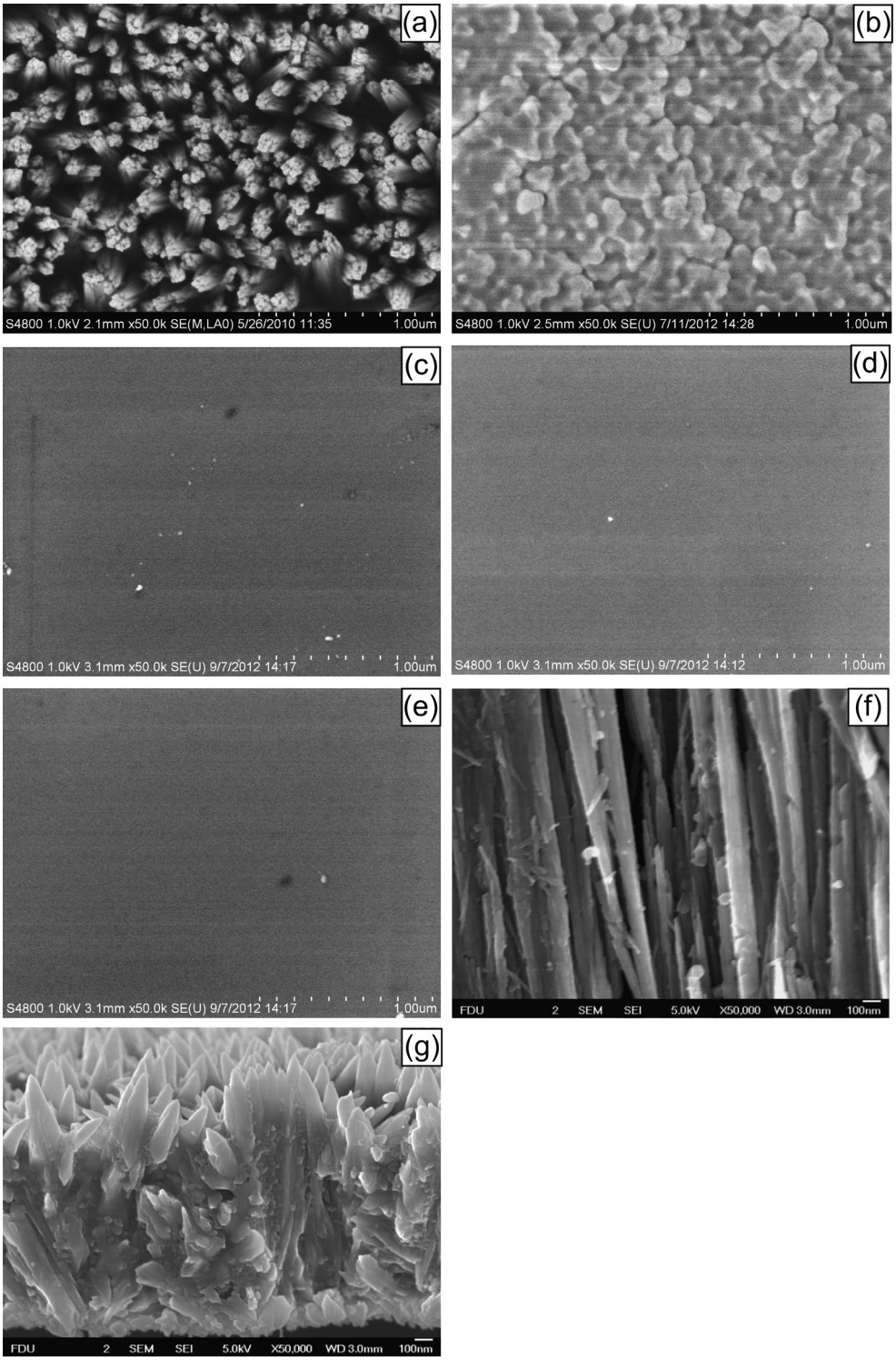

Fig. 1. FE-SEM images of the composites with different Si percentages: (a) 100% TNA, (b) 25% Si, (c) 50% Si, (d) 75% Si, (e) 100% Si, (f) sectional view of TNA, (g) sectional view of Si(75%)/TNA composite.

lattice fringes can be assigned to the interplanar distance of Si (220), which is $d_{220} = 0.195$ nm. The mean grain size measured in TEM image is 1.6 nm, which is in agreement with the aforementioned XRD results. Two kinds of Si phase are identified, which is agreement with Raman data. SAED pattern in Fig. 3(c) confirms the crystalline structure observed in XRD and TEM. The circle pattern indicates that Si is in polycrystalline phase presenting planes (111) and (220).

The distribution of Si in the composites is studied with element analysis mapping at low magnification, as shown in Fig. 4(a–d). From the Si element maps in Fig. 4(d), Si owns the most amount and distributes uniformly in the composites. EDX investigation was carried out in order to confirm the elemental composition of the composites. Only elements Ti, O and Si can be observed. Quantitative analysis in Fig. 4(e) manifests the weight percentage of Si is 76%, which coincides with the composite fabrication process.

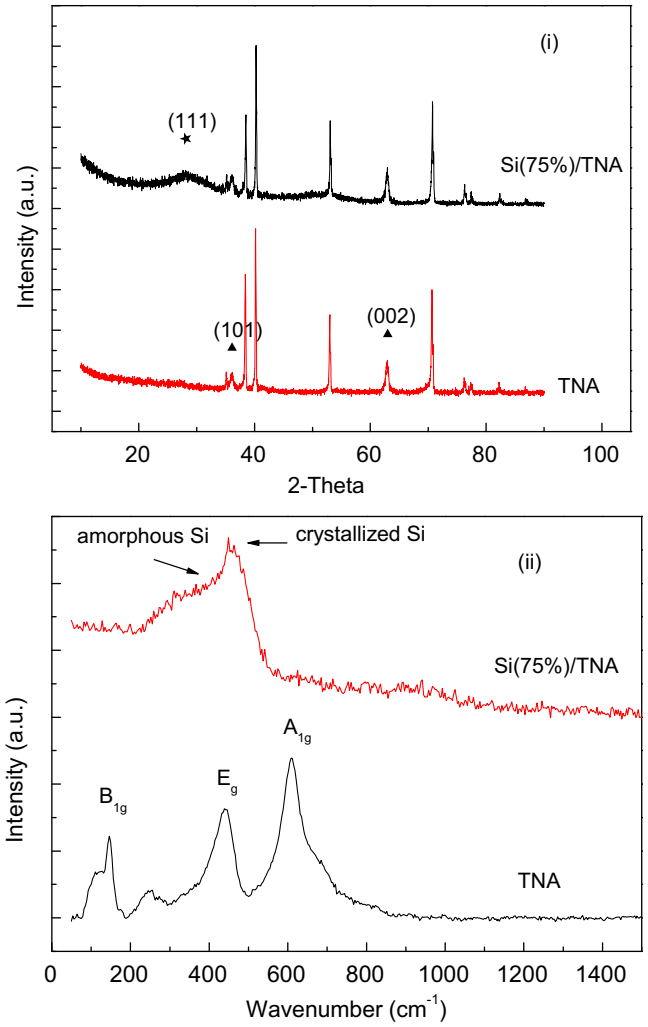

Fig. 2. (i) XRD patterns of TNA and Si/TNA composites with 75% Si content; (ii) Raman spectra of TNA and Si/TNA composites with 75% Si content.

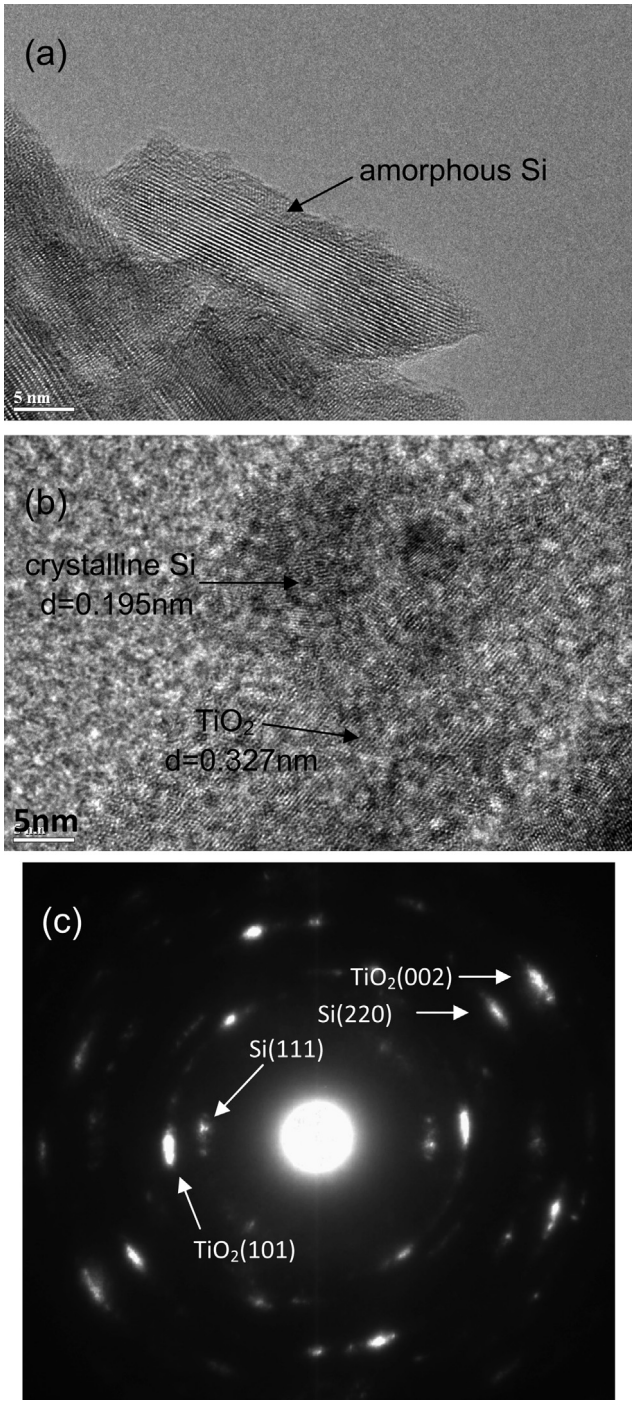

Fig. 3. (a, b) TEM images of Si/TNA composites (c) selected-area electron diffraction pattern.

Charge–discharge measurement was performed to examine the electrochemical behavior of the TiO_2 film and Si/TNA composite, and the voltage–capacity profiles are presented in Fig. 5. The TiO_2 anode is always discharged to 1.0 V in previous works [28,29]. However, considering silicon-based materials are normally discharged to 0 V, in this study TiO_2 is also discharged to 0 V, as shown in Fig. 5(a). A sloping region from 2.4 V to 1.4 V during discharge and charge is visible. The slope behavior is consistent with that of nanosized rutile reported previously [21,30–32], which may be due to the storage of Li on the rutile nanowire surface. In the region below 1.4 V, it corresponds to Li insertion into the TiO_2 bulk [30]. During the first cycle, a total discharge capacity of 228 mA h g^{-1} is achieved with a reversible capacity of 153 mA h g^{-1}, leading to a coulombic efficiency of 67.1%. For TNA/Si composites shown in Fig. 5(b–e), apart from the discharge/charge plateaus of TiO_2, the potential plateau below 1.0 V versus Li/Li^+ is attributed to the intercalation/extraction of Li ion in Si. The composites with Si percentages of 25%, 50%, 75% and 100% show initial discharge capacities of 1332, 1513, 2384, and 1686 mA h g^{-1}, and the corresponding charge capacities are 799, 1132, 1480 and 555 mA h g^{-1}. The respective coulombic efficiencies are 60.0%, 74.8%, 62.1% and 32.9%. Comparing with pure TiO_2, the capacities of TNA/Si composites are improved greatly. Typically the composite with 75% silicon owns the highest reversible capacity and superior coulombic efficiency. The large amount of silicon component affords huge capacity and the steady TiO_2 framework effectively accommodates Si volume expansion, preventing formation of the electronic isolation of silicon particles. The irreversible capacity is attributed to the formation of the solid electrolyte interphase (SEI) layer during the first discharge process and the trapping of the lithium ions in the defected and pulverized silicon particles. By excluding 153 mA h g^{-1} contributed by TiO_2, the first cycle charge capacity delivered by Si is 1327 mA h g^{-1}.

Fig. 6 shows the cycling capacity values for the first 200 cycles. The rutile TNA electrode exhibits a good cycling stability and the

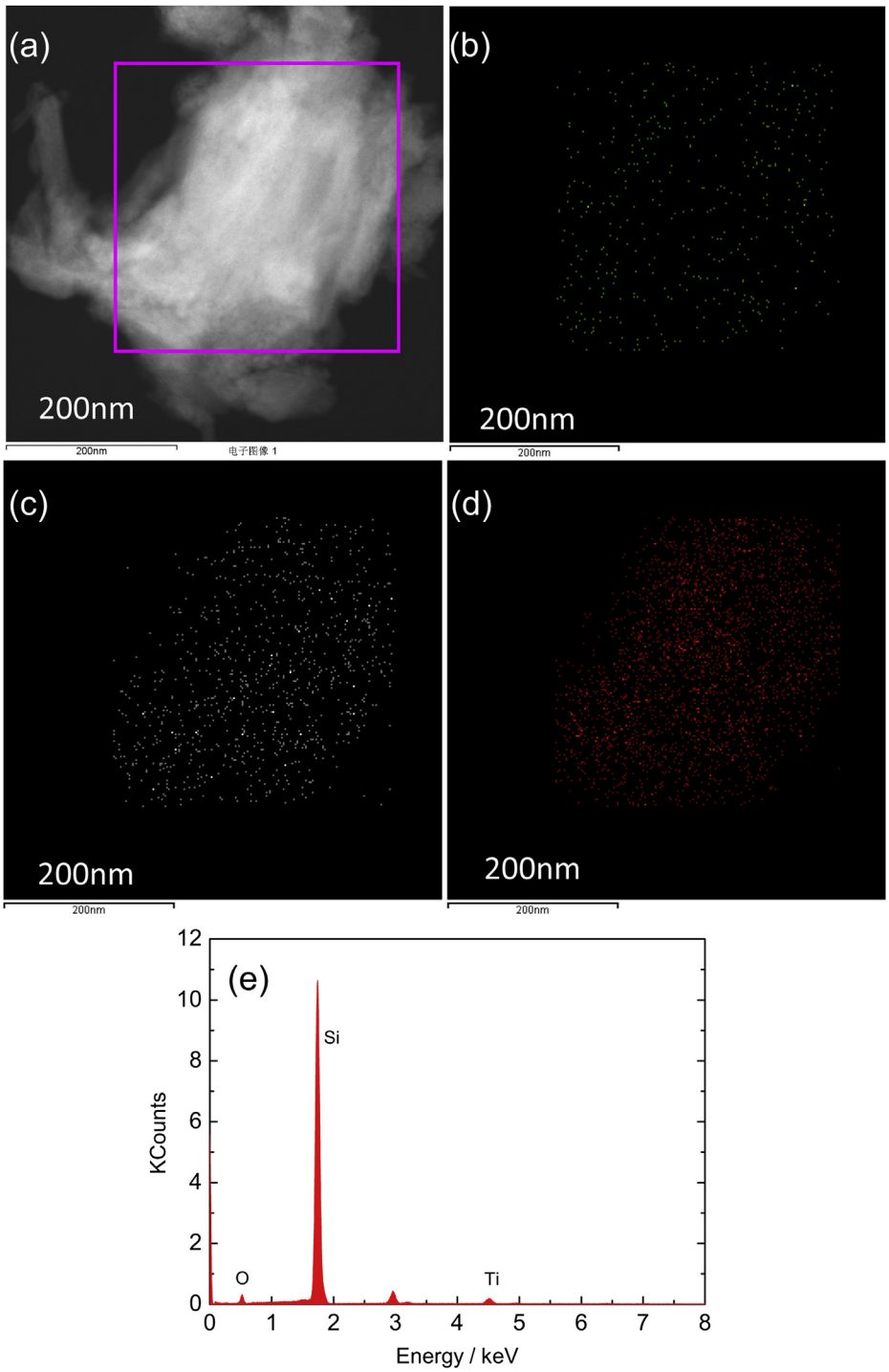

Fig. 4. Element mapping and EDX pattern of the Si/TNA composites with 75% Si content: (b) O, (c) Ti, (d) Si.

charge capacity remains 104.1 mA h g^{-1} after 200 cycles, i.e. 67.6% retention. For Si/TNA composites with 25% and 50% Si content, the charge capacity gradually reduced to 462.4 and 558.2 mA h g^{-1} at the 200th cycle, corresponding to capacity retention of 57.8% and 49.3% respectively. The Si(75%)/TNA composite owns the highest reversible capacity of 1001.3 m Ah g^{-1} after 100 cycles. And after 200 cycles the remaining capacity reaches as high as 802.3 mA h g^{-1}, i.e. 54.2% retention. As for pure Si, charge capacity reduces sharply to 441 mA h g^{-1} at the 3rd cycle and remains at 301.4 mA h g^{-1} after 200 cycles. It illustrates that pure silicon material confronts severe problem of crack and pulverization, leading to rapid capacity fade. In Si/TiO_2 composite structure, Si component is partially embedded into the interspace between TiO_2 nanowires, and the stable TNA framework can effectively prevent Si from cracking and disconnecting with current collector. That's the reason for Si/TNA composite to retain high capacity after 200 cycles. Meanwhile relative high percentage of Si offers high capacity.

Cyclic voltammetry is applied to further illustrate the electrochemical mechanism and contribution of TiO_2 in the prepared Si/TiO_2 thin film. Fig. 7 shows the cyclic voltammetry curves measured

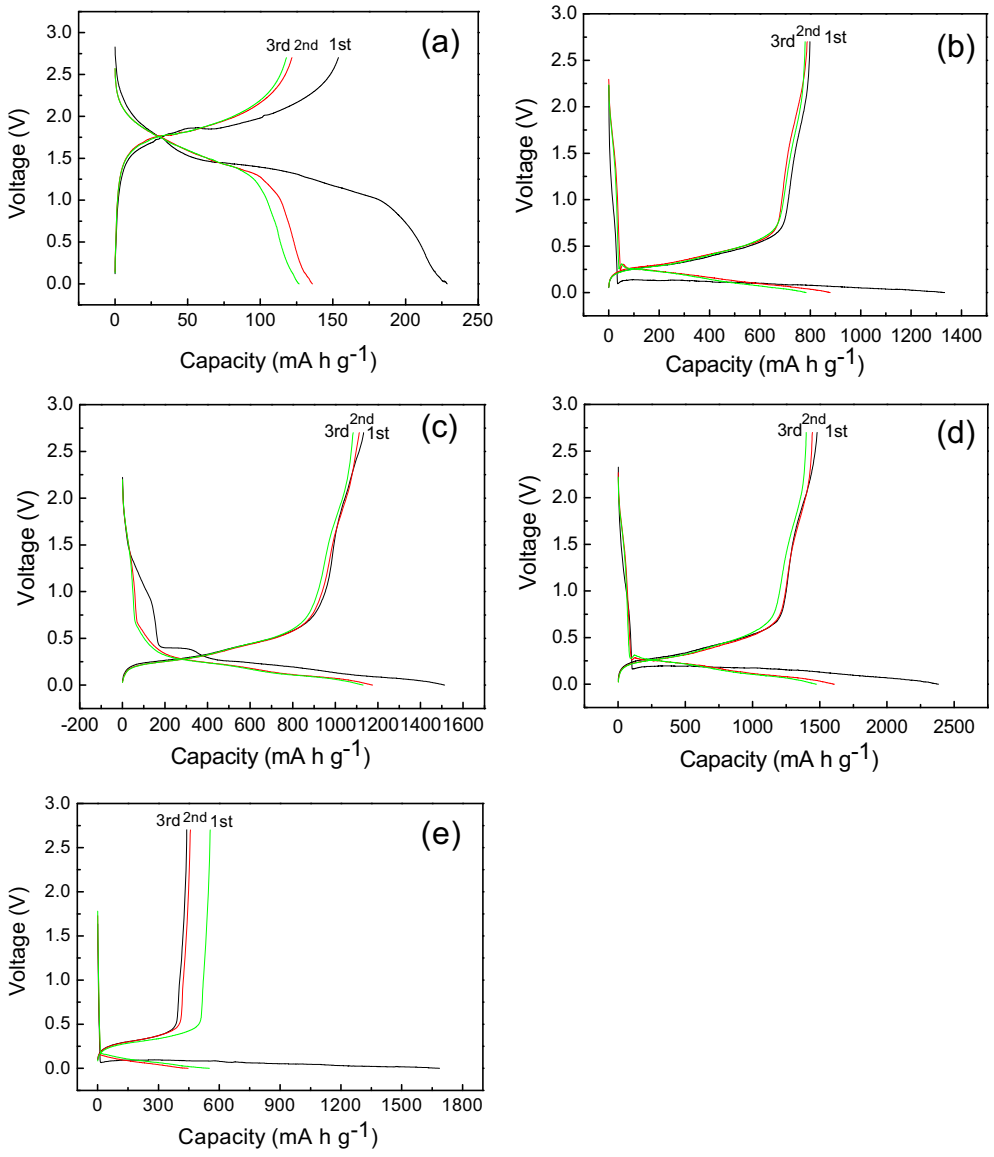

Fig. 5. The initial three cycles' discharge/charge curves of the composites with different Si percentages: (a) 100% TNA, (b) 25% Si, (c) 50% Si, (d) 75% Si, (e) 100% Si.

between 0 and 2.7 V versus Li/Li^+ at a potential scan rate of 0.10 mV s^{-1}. The activated cells were tested for three cycles and the second cycles were chosen to plot CV curves. For pure TiO_2, cathodic peak around 1.55 V and anodic peak around 1.79 V appear,

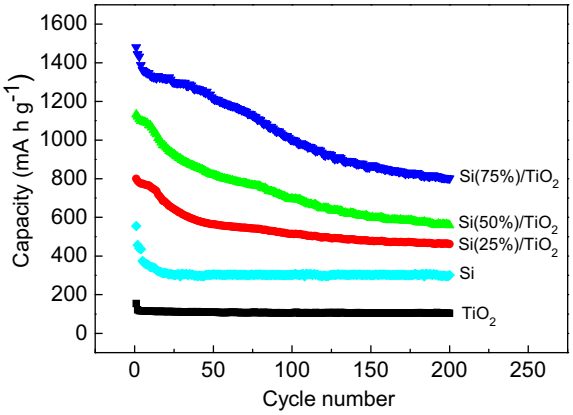

Fig. 6. Cycle behavior of the electrodes made of bare TNA and Si/TNA composites.

which are consistent with the voltage plateau shown in Fig. 5(a). As for the curve of pure Si, sharp reduction peaks appear at 0.19 V and 0.05 V, representing the insertion of Li^+ into silicon. Subsequently, two anodic peaks (lithium extraction) occur at 0.30 V and 0.49 V. These four redox peaks are attributed to the alloying/dealloying process of Li with active Si particles and remain stable, which are in good agreement with the discharge/charge curves shown in Fig. 5.

In the curves of Si/TiO_2 composites, redox peaks of TiO_2 and Si appear simultaneously. With the Si percentage being enhanced from 25% to 75%, peak intensity of Si increases and peak intensity of TiO_2 reduces gradually. The role of TiO_2 plays in the electrochemical mechanism is convincingly proved by the CV data.

To further discuss the electrochemical mechanism, the FE-SEM images of the Si/TNA composites with different Si percentages after 200 discharge/charge cycles are given in Fig. 8. For pure TiO_2, nanowire structure has already disappear, but interspace between nanowires retains, and it becomes a porous structure. As for pure Si, film structure cracks and forms isolate islands. However, for the composites of Si content from 25% to 75%, the silicon film stably exists and no severe mechanical disintegration occurs. Typically in the 75% Si sample, holes in the diameter range of 0.25–2.5 μm

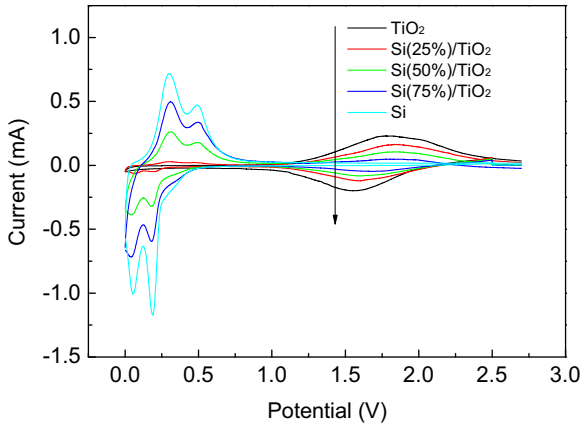

Fig. 7. Cyclic voltammogram plots of bare TNA and Si/TNA composites.

spread uniformly across the film. Silicon film suffers huge volume expansion during the Li-ion insertion procedure, resulting in silicon particles to break off from the film, and silicon particles indeed can be seen on the film. This is probably the formation process of holes and particles. The silicon film retains stably after 200 cycles, and this is a convincing evidence for the excellent cycling performance of the Si/TNA composite.

Fig. 9 reveals the performance of Si/TNA composite with 75% Si content at rates varied from 100 mA g^{-1} to 1600 mA g^{-1}. Reversible capacities of 1567, 1304, 1114, 850 and 536 mA h g^{-1} are achieved at various rates. About 34.2% of the reversible capacity at 100 mA g^{-1} remains while increasing current density to 1600 mA g^{-1}. By reducing current density back to 100 mA g^{-1}, the capacity recover to 1473 mA h g^{-1}, which is about 94.0% of the median-cycle capacity at 100 mA g^{-1}. Capacity decreases rapidly at high current density, however, the capacity recover ability is excellent. The good rate performance can be explained as follows: from XRD and FE-SEM data we can tell TNA grows along (002) crystal plane, i.e. *c*-axis. During the process of Li-insertion into rutile TiO_2, the Li^+ diffusion coefficient is much higher along *c*-axis (10^{-6} cm^2 s^{-1}) than in the ab-planes (10^{-15} cm^2 s^{-1}) [33,34], and also larger than that of vacuum-deposited Si (10^{-13} to 10^{-10} cm^2 s^{-1}) reported by Yoshimura et al. [35]. The TNA structure in this study grows along c-axis, which significantly facilitates Li^+ diffusion. Besides, the Si component is semiconducting, and its conduction is better than TiO_2. These two reasons enable good capability of rapid discharging and charging.

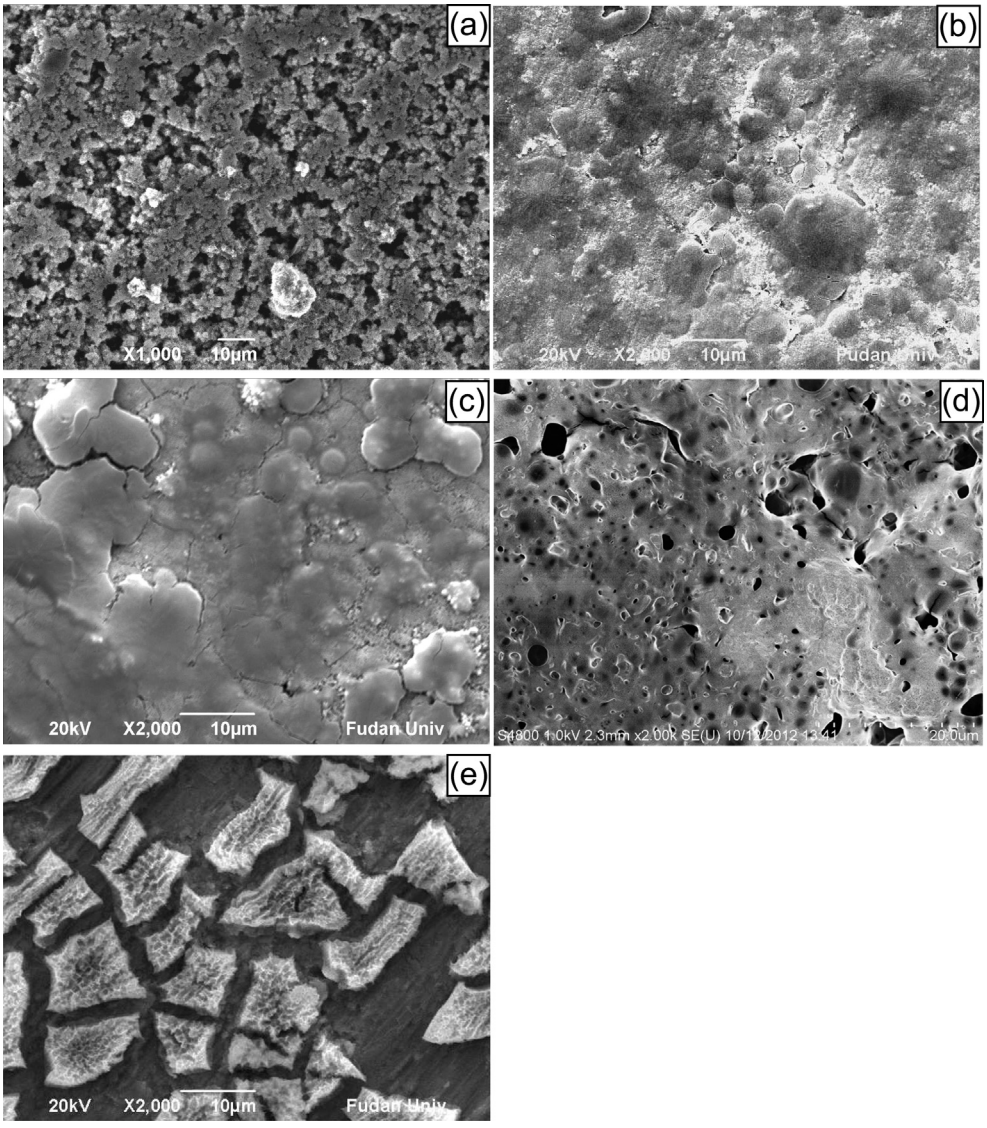

Fig. 8. FE-SEM images of the Si/TNA composites with different Si percentages after 200 cycles: (a) 100% TNA, (b) 25% Si, (c) 50% Si, (d) 75% Si, (e) 100% Si.

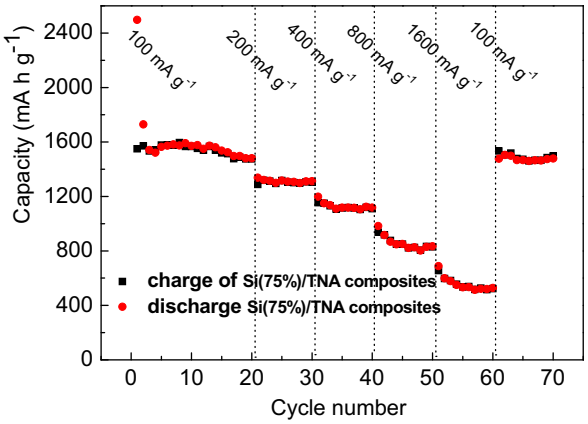

Fig. 9. Rate performance of the Si/TNA composites with 75% Si content.

4. Conclusions

A novel material of Si/TiO_2 nanowire array composite has been fabricated directly on titanium substrate through a facile method. This nanostructure provides good electrical contacts between the active materials and the current collector without using additives and conductive agents. The TNA framework ensures excellent cycling stability of the composite structure, and an appropriate amount of Si brings high specific capacity and good rate capability. The as-prepared Si includes two phases of amorphous and nanocrystalline. Composites with different Si mass percentages are researched, by introducing 75% Si component, the reversible capacity increases significantly to 1480 mA h g^{-1} for the initial cycle. The TiO_2 framework accommodates Si and lessens its mechanical strain during cycling. After 200 cycles, charge capacity remains as high as 802.3 mA h g^{-1}. The crystal growth direction of TNA and also electrical conductivity of Si component facilitate rapid discharge/charge performance. Our study has therefore opened the great possibility for rutile TiO_2 nanowire arrays combined with other high capacity materials to apply in many fields of Li-ion batteries.

Acknowledgement

The authors acknowledge funding supports from the National Natural Science Foundation (No. 21173054) and the National Key Basic Research Program of China (973 Program, Grant No. 2013CB934103).

References

[1] T.D. Hatchard, J.M. Topple, M.D. Fleischauer, J.R. Dahn, Electrochem. Solid-State Lett. 6 (2003) A129–A132.
[2] W.J. Weydanz, M. Wohlfahrt-Mehrens, R.A. Huggins, J. Power Sources 81–82 (1999) 237–242.
[3] Y. Idota, T. Kubota, A. Matsufuji, Y. Maekawa, T. Miyasaka, Science 276 (1997) 1395–1397.
[4] S.D. Beattie, J.R. Dahn, J. Electrochem. Soc. 150 (2003) A894–A898.
[5] P.G. Bruce, B. Scrosati, J.M. Tarascon, Angew. Chem. Int. Ed. 47 (2008) 2930–2946.
[6] D. Deng, M.G. Kim, J.Y. Lee, J. Cho, Energy Environ. Sci. 2 (2009) 818–837.
[7] X.L. Yang, P.C. Zhang, Z.Y. Wen, L.L. Zhang, J. Alloys Compd. 496 (2010) 403–406.
[8] B. Peng, F.Y. Cheng, Z.L. Tao, J. Chen, J. Chem. Phys. 133 (2010) 034701-1–034701-5.
[9] H.X. Li, F.Y. Cheng, Z.Q. Zhu, H.M. Bai, Z.L. Tao, J. Chen, J. Alloys Compd. 509 (2011) 2919–2923.
[10] H. Ma, F.Y. Cheng, J. Chen, J.Z. Zhao, C.S. Li, Z.L. Tao, J. Liang, Adv. Mater. 19 (2007) 4067–4070.
[11] S. Ohara, J. Suzuki, K. Sekine, T. Takamura, J. Power Sources 136 (2004) 303–306.
[12] K. Kang, H.S. Lee, D.W. Han, G.S. Kim, D. Lee, G. Lee, Y.M. Kang, M.H. Jo, Appl. Phys. Lett. 96 (2010) 053110-1–053110-3.
[13] V.A. Sethuraman, K. Kowolik, V. Srinivasan, J. Power Sources 196 (2011) 393–398.
[14] J.W. Kim, J.H. Ryu, K.T. Lee, S.M. Oh, J. Power Sources 147 (2005) 227–233.
[15] D.Q. Shi, J.P. Tu, Y.F. Yuan, H.M. Wu, Y. Li, X.B. Zhao, J. Electrochem Commun. 8 (2006) 1610–1614.
[16] J.G. Tu, W. Wang, S.Q. Jiao, J.G. Hou, K. Huang, H.M. Zhu, Mater. Chem. Phys. 136 (2012) 863–867.
[17] S.E. Park, B.E. Kim, S.W. Lee, J.K. Lee, Trans. Nonferrous Met. Soc. China 19 (2009) 1023–1026.
[18] Y.Q. Zhang, X.H. Xia, X.L. Wang, Y.J. Mai, S.J. Shi, Y.Y. Tang, C.G. Gu, J.P. Tu, J. Power Sources 213 (2012) 106–111.
[19] K.M. Lee, Y.S. Lee, Y.W. Kim, Y.K. Sun, S.M. Lee, J. Alloys Compd. 472 (2009) 461–465.
[20] X.Y. Wang, Z.Y. Wen, Y. Liu, L.Z. Huang, M.F. Wu, J. Alloys Compd. 506 (2010) 317–322.
[21] S.U.M. Khan, M. Al-Shahry, W.B. Ingler, Science 297 (2002) 2243–2245.
[22] M. Wagemaker, G.J. Kearley, A.A. Well, H. Mutka, F.M. Mulder, J. Am. Chem. Soc. 125 (2003) 840–848.
[23] D.H. Wang, D.W. Choi, Z.G. Yang, V.V. Viswanathan, Z.M. Nie, C.M. Wang, Y.J. Song, J.G. Zhang, J. Liu, Chem. Mater. 20 (2008) 3435–3442.
[24] X. Feng, K. Shankar, O.K. Varghese, M. Paulose, T.J. Latempa, C.A. Grimes, Nano Lett. 8 (2008) 3781–3786.
[25] Y.C. Lin, S.H. Liu, H.R. Syu, T.H. Ho, Spectrochim. Acta Part A 95 (2012) 300–304.
[26] J. Bonse, K.W. Brzezinka, A.J. Meixner, Appl. Surf. Sci. 221 (2004) 215–230.
[27] L.Y. Shen, X.W. Guo, X.P. Fang, Z.X. Wang, L.Q. Chen, J. Power Sources 213 (2012) 229–232.
[28] G.F. Ortiz, I. Hanzu, T. Djenizian, P. Lavela, J.L. Tirado, P. Knauth, Chem. Mater. 21 (2009) 63–67.
[29] G.F. Ortiza, I. Hanzua, P. Knautha, P. Lavela, J.L. Tirado, T. Djenizian, Electrochim. Acta 54 (2009) 4262–4268.
[30] Y. Hu, L. Kienle, Y. Guo, J. Maier, Adv. Mater. 18 (2006) 1421–1426.
[31] H. Qiao, Y. Wang, L. Xiao, L. Zhang, Electrochem. Commun. 10 (2008) 1280–1283.
[32] B. Liu, E.S. Aydil, J. Am. Chem. Soc. 131 (2009) 3985–3990.
[33] M.V. Koudriachova, N.M. Harrison, S.W. de Leeuw, Phys. Rev. Lett. 86 (2001) 1275–1278.
[34] M.V. Koudriachova, N.M. Harrison, S.W. de Leeuw, Solid State Ionics 175 (2004) 829–834.
[35] K. Yoshimura, J. Suzuki, K. Sekine, T. Takamura, J. Power Sources 146 (2005) 445–447.